ACS Sustainable Chemistry & Engineering

Research Article

Cite This: ACS Sustainable Chem. Eng. 2018, 6, 11286−11294

pubs.acs.org/journal/ascecg

Solution Processed Hafnia Nanoaggregates: Influence of Surface Oxygen on Catalytic Soot Oxidation

Devika Laishram, Kiran P. Shejale, Ritu Gupta,* and Rakesh K. Sharma*

Department of Chemistry, Indian Institute of Technology Jodhpur, NH-65, Karwar, Jodhpur 342037, Rajasthan, India

Supporting Information

ABSTRACT: Hafnium dioxide (HfO_2) nanoaggregates are synthesized by sol−gel and hydrothermal routes followed by hydrogen annealing at different time durations. The proposed study aims to explore the effect of hydrogen annealing time on the properties of HfO_2 and also envisage the catalytic soot oxidation using HfO_2 nanoaggregates. It is observed that annealing under a hydrogen atmosphere brought about substantial changes in certain attributes such as chemical and textural properties with marginal changes in some other properties like optical activity and band gap. The pristine HfO_2 without hydrogen annealing showed a lower ignition temperature, whereas hydrogen annealed HfO_2 for 2 h showed the best catalytic performance characterized by the soot combustion temperature (T_{50}) in contrast to samples prepared at longer duration because of the higher surface adsorbed oxygen species in its widely distributed pores.

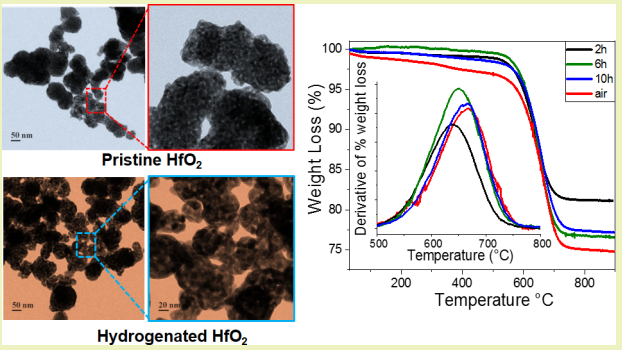

KEYWORDS: *HfO_2, Hydrogen annealing, Soot oxidation, Mesoporous nanostructure, TGA*

INTRODUCTION

Nanostructured materials have marked an important era in science, technology, and engineering with their exclusive properties. Hafnium oxide or hafnia (HfO_2) is chemically, mechanically, and thermally stable and exhibits a high melting point (2758 °C)[1] with a high dielectric constant ($k \approx 25$).[2,3] It is a wide band gap (>5 eV) material having a high refractive index and has been used extensively as antireflection coatings and optical coating for interference filters.[4−8] HfO_2 exists in various polymorphs such as cubic, tetragonal, orthorhombic, and monoclinic phases.[9] Under normal temperature and pressure, the monoclinic phase shows optimum stability and changes to the metastable tetragonal phase at temperatures greater than 1700 °C and to the cubic phase beyond 2600 °C.[2] Moreover, HfO_2 is a high density material (~10 g/cm^3), which along with activation with other material (like Eu^{3+}) make good scintillating materials[10] and thermal barrier coatings for operation in harsh and high temperature environments.[11] Hafnia is also used for coatings for energy efficient window systems and also in UV mirrors and laser windows due to enhancement of threshold damage.[4,11,12] It is an attractive option for gate insulators in the nanoelectronics and microelectronics industry because of its low leakage current.[13,14] However, studies involving HfO_2 nanocrystals as catalysts are limited due to low porosity, less surface area, and high density compared to other catalytic materials.[15,16] Tailoring of size, morphology, and the surface at the nanoscale could enhance properties such as surface area to volume ratio, porosity, and catalytic activity as well as electrical, optical, and mechanical properties, which will be helpful to further promote the use of HfO_2 as a catalyst in applications such as soot oxidation.

Of the many methods available for the synthesis of doped and pure HfO_2, the hydrothermal method[17,18] is the preferred method for synthesis under milder conditions. Moreover, properties like size, shape, and morphology of the nanomaterial can be controlled by varying reaction conditions such as time, temperature, pressure, solvents, and pH of the reaction.[19−21] The synthesized material is annealed under hydrogen for varying time intervals to passivate dangling bonds and remove native oxygen from the HfO_2 surface.[22] Recent studies revealed that HfO_2 films upon hydrogen annealing exhibit lower electrical resistivity with improved crystallinity[23] without a considerable change in the optical properties.[23]

In the literature, catalytic soot oxidation pertaining to metal oxides is mainly focused on transition metal,[24] perovskites,[25] and ceria.[26] The only example reported to HfO_2 based soot oxidation is in combination with CeO_2 where HfO_2 was used for enhancing textural stability.[27,28] A comprehensive literature survey of various materials used for soot oxidation is provided in the Supporting Information, Table S1. Herein, we report a new unconventional synthetic protocol to prepare HfO_2 with high porosity and surface area to be used for catalytic applications. We have utilized HfO_2 as a support system for

Received: February 9, 2018
Revised: June 23, 2018
Published: July 16, 2018

DOI: 10.1021/acssuschemeng.8b00674
ACS Sustainable Chem. Eng. 2018, 6, 11286−11294

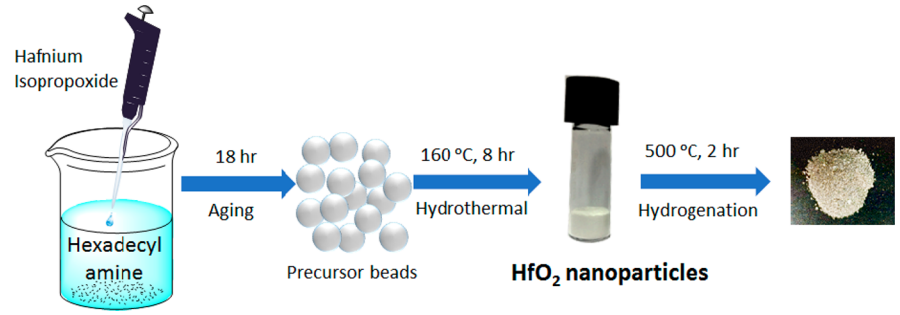

Figure 1. Schematic demonstrating the synthesis of HfO_2 solid nanosphere aggregates by sol−gel and hydrothermal methods.

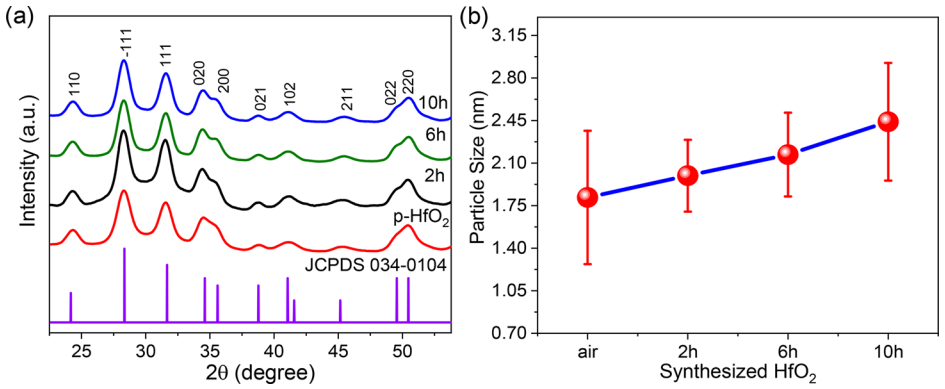

Figure 2. (a) XRD patterns of p-HfO_2 nanoparticles annealed in air and H-HfO_2_2h, H-HfO_2_6h, and H-HfO_2_10h. (b) Plot showing variation in particle size of the synthesized HfO_2 nanoaggregates.

catalytic oxidation and investigated the role of surface oxygen by comparing the pristine with hydrogenated HfO_2. This study further aims to supplement our previous reported data where 1% of HfO_2 doped in TiO_2 is hydrogenated resulting in high current density (J_{SC}) and increased efficiency of dye-sensitized solar cells.[29] In this, nanohafnia is prepared by a two-step process involving a sol−gel and hydrothermal route followed by annealing under hydrogen for different time intervals. The HfO_2 was then characterized by various methods to study the influence of hydrogen annealing on structural, optical, and catalytic properties.

EXPERIMENTAL SECTION

Synthesis of HfO_2 Nanoparticles. HfO_2 and H-HfO_2 nanospheres were prepared via a modified sol−gel process followed by hydrothermal treatment.[29] Hafnium propoxide (HIP) (40 mM) was added dropwise into a mixture of 200 mL of ethanol and 1.975 g of hexadecylamine (HDA) under vigorous stirring. The mixture was kept in the dark for 18 h and then filtered. The filtered white precipitate was dried under air at room temperature and crushed to get a fine powder. The crushed powder (0.8 g) is dispersed in 10 mL of ethanol, 5 mL of deionized water (DI), and 0.25 mL of liquor ammonia by ultrasonication for 10 min. The mixture is then transferred to a Teflon-lined steel autoclave and kept for 8 h at 160 °C in a preheated oven. After the completion of the reaction, the resultant product was filtered and washed repeatedly with DI water followed by absolute ethanol before drying in a vacuum oven at 70 °C overnight. The obtained sample was subsequently ground in a mortar pestle and annealed in a tubular furnace at 500 °C for 2 h in air to obtain a white colored pristine HfO_2 (p-HfO_2). Similarly, samples were annealed for different time intervals at 2, 6, and 10 h under a gas flow of 10% H_2 and 90% N_2 for 500 °C at a heating rate of 2.5 °C min^{-1} to get off-white colored H-HfO_2 nanoaggregates (Figure S1). The HfO_2 solid nanosphere aggregates were prepared by a combination of sol−gel and hydrothermal processes. In the foremost sol−gel step, HfO_2 precursor beads were prepared by mixing the HfO_2 precursor with hexadecylamine (HDA) in an alcoholic solution. The interaction between the hydrolyzed HIP molecules and amine group of HDA results in the formation of organic−inorganic oligomers with HDA acting as a structure directing agent. These oligomers polymerize, condense, and precipitate, leading to the formation of HfO_2 precursor beads. These precursor beads undergo a hydrothermal treatment in the next step to give nanoaggregates of HfO_2. Finally, the powdered nanoaggregates are annealed at 500 °C in air for 2 h resulting in HfO_2 nanoaggregates referred to as p-HfO_2, and these were hydrogenated by annealing under H_2 at 500 °C for different time intervals (2, 6, and 10 h) and designated as H-HfO_2_2h, H-HfO_2_6h, and H-HfO_2_10h, respectively. A schematic illustration of the synthesis process is given in Figure 1.

Characterization. The synthesized nanoaggregates were subjected to powder X-ray diffraction (XRD) analysis using a Bruker D8 Advance Diffractometer with a Cu Kα wavelength of 1.54 Å. TEM imaging was performed by transmission electron microscope (FEI Tecnai-G2 T20). For imaging, ∼10 mg of the sample was dispersed in ethanol and drop coated on a copper grid and allowed to dry before imaging. Diffuse reflectance spectra were recorded using a UV−vis spectrophotometer (Varian Cary 4000) over a wavelength range of 200−800 nm. Here, PTFE (poly tetrafluoroethylene) was used as the standard material for baseline correction. HRTEM images were analyzed with ImageJ and Gatan Digital Micrograph software. The surface composition and chemical states were measured with an Omicron Nanotechnology (Oxford Instruments) X-ray photoelectron spectroscope (XPS) equipped with monochromatic Al Kα radiation. The peak correction with respect to the adventitious carbon peak is done for Hf 4f and O 1s by a shift correction factor of 4.8 eV with reference to a standard carbon 1s peak obtained at 284.6 eV.[30] The XPS spectra were fitted by means of a Gaussian function after a Shirley background subtraction. A BET adsorption−desorption isotherm was performed to understand the effect of hydrogenation on the porosity of the HfO_2 solid nanosphere aggregates. The specific surface area was analyzed by BET, and the pore volume and geometry were analyzed by BJH analysis using an N_2 adsorption−desorption

DOI: 10.1021/acssuschemeng.8b00674
ACS Sustainable Chem. Eng. 2018, 6, 11286−11294

isotherm (Quntachrome Autosorb iQ$_3$) with 0.05 error values for all of the measurements. Temperature-programmed desorption (TPD) experiments were performed using an Autochem 2920 Micromeritics Chemisorptions Analyzer.

Soot Oxidation Activity. Catalytic soot oxidation activity was measured by thermogravimetric (TGA) analysis in a PerkinElmer, Simultaneous Thermal Analyzer (STA) equipped with a digital temperature controller from PolyScience. The model soot used for this study was carbon black (acetylene black) obtained from Alfa Aesar (1333-86-4). The weight loss measurement of the catalyst/soot mixture at a 4:1 ratio was studied in the temperature range from 30 to 900 °C under zero air at a 10 °C/min heating rate with an air flow rate of 20 mL/min. The contact between the catalyst and soot plays a vital role, and the catalytic activity depends strongly on the interaction between the two solids and air. Tight contacts have been maintained by grinding the soot and catalyst in a mortar; this is important for the transfer of active oxygen with a catalyst surface and soot particles. Figure 8a represents the schematic for the measurement of soot oxidation activity.

RESULTS AND DISCUSSION

Structural Analysis. *XRD Analysis.* The XRD patterns of pristine and hydrogen annealed HfO_2 nanoaggregates are shown in Figure 2a; the patterns correspond to the monoclinic phase of HfO_2, and all of the peaks are identified and indexed accordingly as per JCPDS data card no. 034−0104. Further, no other secondary peaks were observed, indicating that the as-synthesized HfO_2 is of pure phase. The most prominent peak of HfO_2 matches the $(\bar{1}11)$ monoclinic phase of HfO_2, which is evident at 2θ equal to 28.2°.[31] H-HfO_2 showed a successive increase in peak intensity, with a 2θ shift toward a lower angle corresponding to higher d-spacing (Figure S2a). Additionally, an increase in average crystallite size can be observed as a result of hydrogen gulping by HfO_2 particles upon annealing for higher duration (2 h < 6 h < 10 h) as shown in Figure 2b. It was also found that the observed peak intensity is highest for H-HfO_2_2h and decreases with an increase in annealing time, which might be because of texturing in the crystal lattice. Furthermore, it was observed that the particle size (calculated from the Williamson Hall method) and the lattice strain increases with increase in annealing time under an H_2 atmosphere and is highest for H-HfO_2_10h nanoaggregates (Table 1, Figure S2b). The strain states increase as H-HfO_2_2h < p-HfO_2 < H-HfO_2_2h < H-HfO_2_6h < H-HfO_2_10h. This is a consequence of prolonged annealing under reduced ambience, leading to introduction of H_2 in the lattice of HfO_2, which creates structural defects and oxygen vacancies in higher concentration.[32] Thus, the increased lattice strain (Figure S2b) for hydrogen annealed HfO_2 nanoaggregates is a result of the increase in the grain boundaries and defects present. Annealing under reduced atmosphere imposes strain upon the Hf lattice, which affects the oxygen vacancy formation and surface chemical activity of the synthesized HfO_2 nanoaggregates. Thus, the increase in lattice strain is likely to affect the adsorption capability and binding ability of the adsorbates strongly. The effect of strain upon the synthesized HfO_2 nanoaggregates were determined by means of a Williamson Hall plot (Figure S3). A plot of catalytic activity and strain for all the synthesized nanoaggregates is given in the SI, Figure S4. Chaubey et al. reports poor crystallization of HfO_2 nanoparticles under a reducing atmosphere (10% H_2 in N_2) at 500 °C temperature for 4 h.[33] Contrarily, the synthesized HfO_2 showed uniform crystallinity for the entire annealing time range from 2 to 10 h under a reducing atmosphere. However, it is interesting to observe the decrease in crystallite size for all of the hydrogen annealed HfO_2 compared to the air annealed pristine p-HfO_2 (Figure 2b and Table 1), as reported elsewhere.[34]

Table 1. Particle Size, *d*-Spacing, and Strain Calculated for the Hydrogenated HfO_2

sample	particle size (nm)	*d*-spacing (Å)	strain (%)
p-HfO_2	1.82	3.15	0.89
H-HfO_2_2h	2.00	3.15	0.69
H-HfO_2_6h	2.17	3.15	1.05
H-HfO_2_10h	2.44	3.15	1.49

Textural Analysis. *TEM Analysis.* TEM images show nanoaggregates of ∼50−100 nm consisting of loosely bound nanoparticles (∼5−10 nm) resembling a bunch of grapes. The size observed under TEM is different from that calculated from XRD probably because of the aggregated nature of nanoparticles.[35] As observed from the TEM images, Figure 3a−c, the interparticle pore widening takes place up on hydrogen annealing. The average size of the HfO_2 aggregate as well as nanoparticles visibly increase upon successively increasing hydrogen annealing from 2 to 6 h. As seen from HRTEM images, interplanar spacing is well-resolved for some of the non-overlapping nanoparticles because of expansion of the aggregated structure upon hydrogenation as seen for 6h_hydrogen annealed HfO_2 in Figure 3f. Also, disordering of the crystal lattice as indicated by the encircled dotted lines is observed because of the introduction of hydrogen into the HfO_2 lattice (Figure 3e,f) as compared to the pristine case (Figure 3d). The $(\bar{1}11)$ oriented HfO_2 nanoparticles ($d \approx 0.31$ nm) corresponding to the monoclinic phase could be easily identified in the HRTEM images as well. Also, the sharp dotted rings of the SAED (selected area electron diffraction)

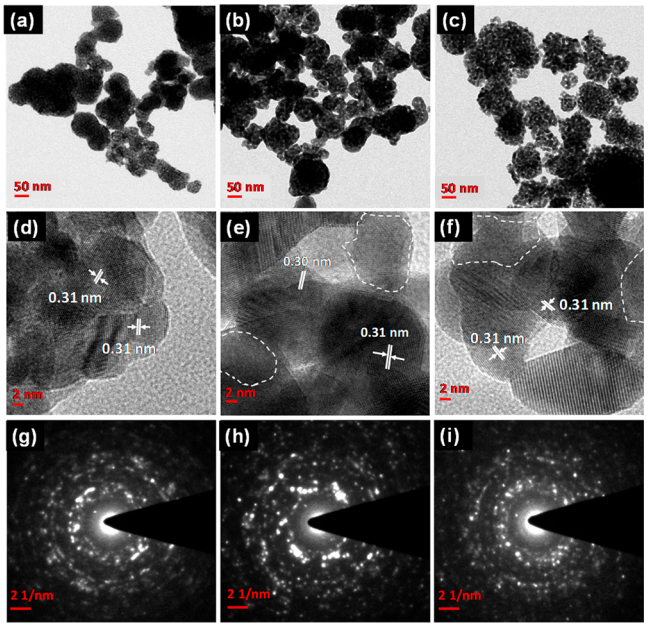

Figure 3. TEM and HRTEM images of air annealed HfO_2 (a,d), 2 h (b,e), and 6 h (c,f) hydrogen annealed HfO_2. The SAED patterns of air annealed (g) and hydrogen annealed 2 h (h) and 6 h (i) samples, respectively, indicating the polycrystalline nature of HfO_2.

DOI: 10.1021/acssuschemeng.8b00674
ACS Sustainable Chem. Eng. 2018, 6, 11286−11294

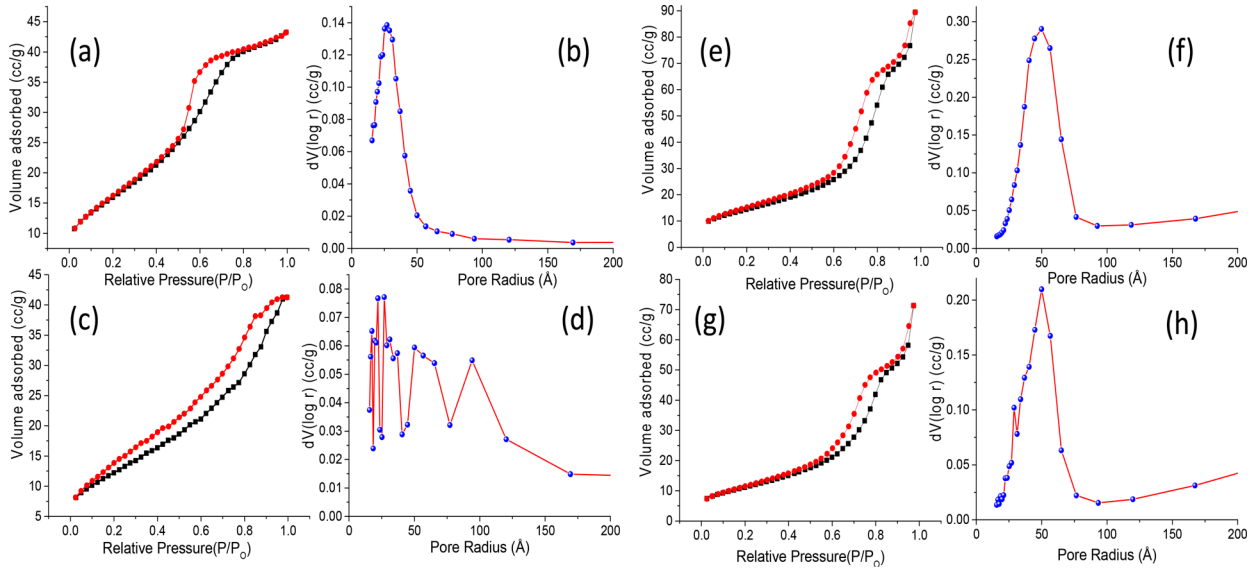

Figure 4. BET adsorption−desorption isotherm and pore size desorption curve for p-HfO_2 (a,b), H-HfO_2_2h (c,d), H-HfO_2_6h (e,f), and H-HfO_2_10h (g,h), respectively.

pattern (Figure 3g−i) indicate that the polycrystalline and disordered nature of HfO_2 increases upon H_2 annealing.

BET Analysis. In order to further understand the nature and geometry of the pores formed, BET adsorption−desorption isotherms were studied and analyzed for the as-synthesized p-HfO_2, H-HfO_2_2h, H-HfO_2_6h, and H-HfO_2_10h nanoparticles. The presence of the broad and wide hysteresis loop with a delay in the condensation−evaporation process is due to the porous nature of the material.[36] The adsorption curves show an early initial monolayer coverage followed by multilayer formation as observed in Figure 4 for all of the synthesized nanomaterials. The p-HfO_2 (Figure 4a) suggests the existence of the "ink bottleneck" type of pores following H2 hysteresis of the IUPAC classification.[37−40] The adsorption isotherm increases gradually until a relative P/P_0 of 0.6 followed by a change in slope at the curve beyond 0.6, which is attributable to the condensation taking place at the neck and the interconnected inner-bottled structure, respectively. However, the desorption curve of this isotherm tracked a delayed curve during the evaporation process up to 0.6 P/P_0 and beyond 0.6 of the neck and inner bottle correspondingly. The delay in such a case might be the effect of pore blocking because of the presence of the interconnected network of the ink bottleneck-like pore structures. The pore size distribution calculated from the BJH desorption curve and was found to be ∼0.054 cc/g with a pore radius of ∼2.5 nm as shown in Figure 4b. Also, the hysteresis loop for p-HfO_2 Figure 4a is associated with a type-IV isotherm indicating capillary condensation in mesopores with a surface area of 57.81 m^2/g. The hydrogen annealed H-HfO_2_2h nanoparticles, unlike p-HfO_2, followed a type-III BET isotherm with a mixed type H2+H3 hysteresis loop as shown in Figure 4c.[36,41] It signals that the unrestricted multilayer formation as the lateral interaction between the adsorbed molecules show stronger interaction compared to the adsorbate and the adsorbent surface. Additionally, it can be inferred that the pores in this case have a narrow (∼1.5 nm radius) bottleneck type of pores along with plate-like lamellar aggregates forming slit porous nanostructures. The BJH pore size distribution is rather broad with pore sizes ranging from 1.5 to 17 nm with no definite maxima (Figure 4d). A slight decrease in pore volume (0.052 cc/g) was observed with a surface area of 44.95 m^2/g. This also agrees well with the observed changes in the TEM images in Figure 3b,c. As the annealing temperature increases to 6 and 10 h, the type of isotherms start to conform to a similar type-V isotherm following H3 hysteresis behavior as given in Figure 4e,g. The pore radius at this point increases to 4.4 and 4.9 nm for H-HfO_2_6h and H-HfO_2_10h, respectively, as shown in Figure 4f,h. The detail pore size and surface area values were evaluated and are presented in Table 2. The increase in pore radius indicates swelling of particles as observed virtually under the TEM (Figure 3c). Similar observations can be made in XRD, where the strain % increases with an increase in annealing time. The type-V isotherm at higher P/P_0 is associated with molecular clustering and pore filling observed in microporous and mesoporous adsorbents. In this work, BJH analysis is used for the determination of pore size. Since N_2 is used as the adsorbate with a cross-sectional area of 16.2 $Å^2$/molecule, BJH analysis is valid for mesopores with pore sizes between 2 and 50 nm. The pore size for pristine HfO_2 is slightly less than 2 nm and becomes ∼4.9 nm upon hydrogen annealing for 10 h.

Table 2. Surface Properties of HfO_2 Air, 2 h, 6 h, and 10 h Samples from BET Analysis

sl. no.	sample name	surface area (m^2/g)	pore volume (cc/g)	pore radius (Å)
1	p-HfO_2	57.81	0.05	25.22
2	H-HfO_2_2h	44.95	0.05	17.50
3	H-HfO_2_6h	51.76	0.47	44.59
4	H-HfO_2_10h	40.88	0.67	49.99

Chemical Analysis. *XPS Analysis.* To study the chemical bonding of the synthesized HfO_2 and the effect of different annealing atmosphere, XPS analysis was performed. HfO_2 being highly insulating in nature showed a charging effect and hence a shift in the peak toward higher binding energy. The Hf 4f spectra for p-HfO_2 and hydrogenated-HfO_2 were fitted to three and four curves, respectively, corresponding to

DOI: 10.1021/acssuschemeng.8b00674
ACS Sustainable Chem. Eng. 2018, 6, 11286−11294

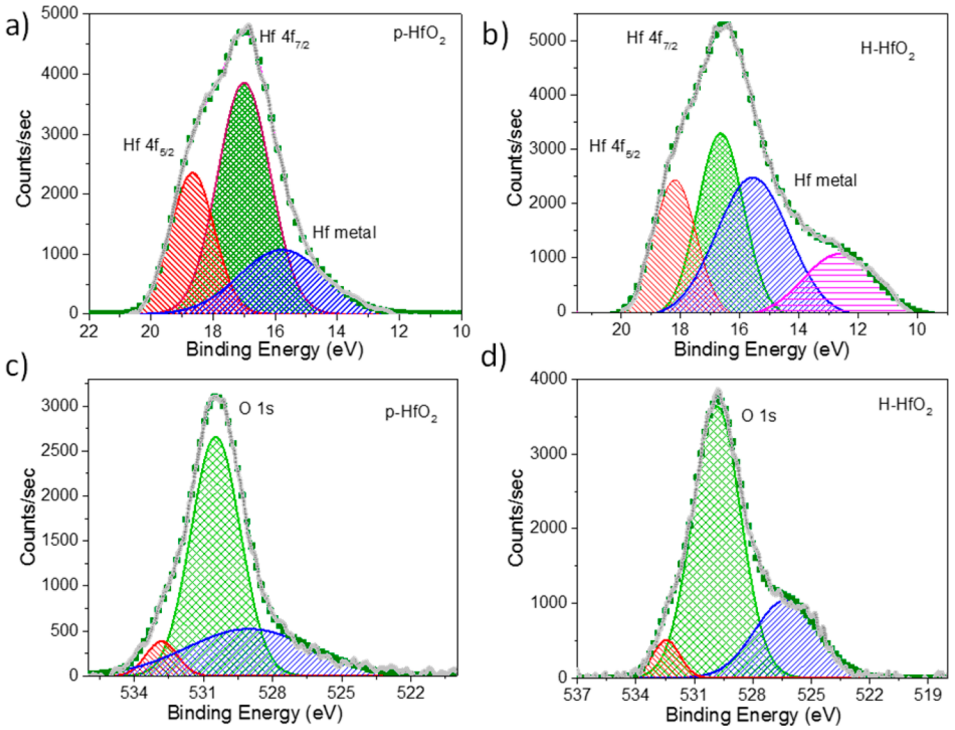

Figure 5. X-ray photoelectron spectra (XPS) of Hf 4f and O 1s in (a,c) pristine and (b,d) hydrogenated HfO_2, respectively. The background subtracted raw experimental data is deconvoluted for identifying the peak contributions of Hf metal and suboxides.

Hf $4f_{7/2}$ and Hf $4f_{5/2}$ peak levels for dioxides and suboxides (Figure 5a,b). The peak area ratios of $j = 5/2$ and $j = 7/2$ were kept at 1.4, and the binding energy difference value of 1.7 eV was kept constant. The observed peaks have large width (>0.9 eV) and hence can be assigned to suboxide and completely oxidized Hf^{4+} (Table 3). The major peaks for p-HfO_2 and H-HfO_2 at 16.99 and 16.64 eV correspond to Hf $4f_{7/2}$, and the shoulder peak at 18.65 and 18.19 eV corresponds to Hf $4f_{5/2}$. The presence of a peak at binding energies of 16.64 and 16.99 eV for the Hf $4f_{7/2}$ levels has been suggested as Hf^{2+} from HfO.[42] The observed chemical shift in hydrogenated-HfO_2 can be attributed to the removal of oxygen species during hydrogen annealing, creating a change in the bonding environment. Thus, it can be inferred that the Hf 4f in H-HfO_2 must have partially reduced ions of Hf, which could increase the redox activity and the catalytic activity because of its mixed oxidation states. Peaks occurring at 15.78 and 15.56 eV can be correlated to presence of suboxide species.[43] These values are nearly in accordance to the reported values in the literature.[44] The O 1s core level peak showed shifting in the binding energy for the air and hydrogen annealed HfO_2 nanoparticle (Figure 5c,d). Each of the peaks is split into three peaks by means of Gaussian peak fitting. The O 1s spectra can be identified with features of chemisorbed oxygen (O_α) and lattice oxygen (O_β) species. The oxygen species present corresponding to binding energies 530.47−529.85 eV can be attributed to the adsorbed surface oxygen or defect oxygen species on the oxygen vacancies ($O_{\alpha1}$), while the binding energies at 532.81−532.43 eV can be ascribed to the adsorbed oxygen species from the hydroxyl group and adsorbed molecular water species ($O_{\alpha2}$).[45] On the other hand, the oxygen species present at the lower binding energies of 529.02−526.28 eV is credited to the presence of lattice oxygen (O_β). The amount of surface oxygen present is quantified (Table 4) as the ratio of the peak area of $O_{\alpha1}$ and O_β ($O_{\alpha1}/O_\beta$).[46] It was observed that the hydrogenated HfO_2 has higher $O_{\alpha1}/O_\beta$ than air annealed HfO_2 by a value of 0.61. Thus, it can be confirmed that even though the air annealed HfO_2 has higher lattice oxygen species present, the hydrogenated HfO_2 overall has higher surface adsorbed oxygen species and therefore might be a beneficial catalyst for exploring soot oxidation activity.

Table 3. Binding Energy of O 1s and Hf 4f Core Levels for p-HfO_2 and H-HfO_2

	p-HfO_2		H-HfO_2	
signal	B.E. (eV)	fwhm (eV)	B.E. (eV)	fwhm (eV)
$O_{\alpha2}$	532.8	1.6	532.4	1.6
$O_{\alpha1}$	530.5	2.5	529.8	2.9
O_β	529.0	6.3	526.3	3.8
Hf $4f_{7/2}$	17.0	2.0	16.6	1.8
Hf $4f_{5/2}$	18.7	1.6	18.2	1.7
Hf^{x+} (suboxides)	15.8	3.2	15.6	2.9
Hf^0 (metal, bulk)	-	-	12.6	2.9

[a]Note: B.E. = binding energy, fwhm = full width half maxima.

Table 4. Surface Oxygen Species Present in the Air and Hydrogen Annealed HfO_2

sample	$O_{\alpha2}$ (%)	$O_{\alpha1}$ (%)	O_β (%)	$O_{\alpha1}/O_\beta$
p-HfO_2	5.8	63.1	31.1	2.0
H-HfO_2_6h	5.3	68.7	25.9	2.6

[a]Note: $O_{\alpha2}$, $O_{\alpha1}$, and O_β percentages are calculated from the percentage area under the respective peaks.

O_2 Temperature-Programmed Desorption (O_2-TPD). The O_2 TPD measurement was done to further investigate the oxygen species in the pristine and hydrogenated HfO_2 as

DOI: 10.1021/acssuschemeng.8b00674
ACS Sustainable Chem. Eng. 2018, 6, 11286−11294

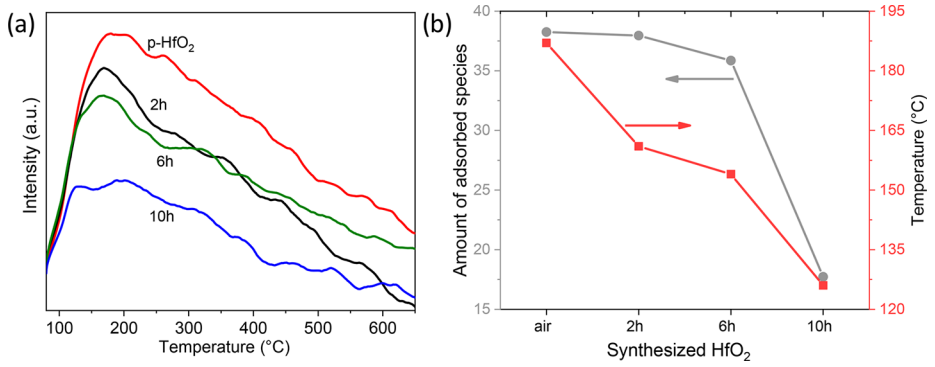

Figure 6. (a) O_2-TPD profile and (b) desorption peak temperature for adsorbed oxygen calculated from peak for HfO_2 nanoaggregate samples.

shown in Figure 6a. According to the literature reports, the oxygen species desorbed at a temperature less than 300 °C can be categorized as O_α; these are active surface adsorbed species and corroborate well with the XPS result. Meanwhile, peaks appearing after 300 °C can be assigned to lattice oxygen (O_β) desorption and are ascribed to the release of oxygen from the lattice in oxide material.[47,48] The absence of O_β is understandable, as the lattice oxygen in HfO_2 is not mobile enough to participate in the oxidation process. Broad peaks are observed at temperatures less than 120−190 °C, corresponding to the surface active oxygen (O_2^- and O^-) species as a result of chemical adsorption. These are the main reactive species in catalytic oxidation reaction because of its labile nature.[49,50] The detailed parameters of the study are given in Table S2. Hydrogenated HfO_2 results in a decrease in the amount of adsorbed species (as seen by the decrease in peak area) with a drop in desorption temperature as shown in Figure 6b. The drop in desorption temperature follow similar trend as that of the increase in lattice strain (Figure S2b) in H-HfO_2 nanoaggregates which suggests that lattice strain caused by hydrogenation changes the surface and binding behavior in the synthesized samples.

Activity Test. *Soot Oxidation Activity.* A comparison weight loss curve of pristine and hydrogenated HfO_2 nanoaggregates is shown in Figure 7. The weight change profile shows a decrease in slope below 100 °C, which can be attributed to the decomposition of water and other organics. This step is followed by saturation (only ∼1% decrease), leaving the mass of the original HfO_2 nearly constant, which indicates the stability of HfO_2 over a wide range of temperatures.

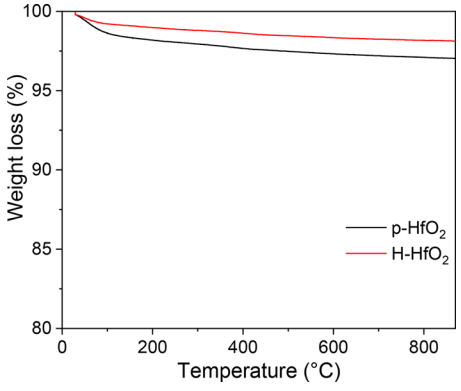

Figure 7. Thermogravimetric analysis of pristine and hydrogenated HfO_2.

The as-synthesized p-HfO_2 and H-HfO_2 samples were used for analyzing the soot oxidation activity because of its fine particle size and highly porous structure. The soot oxidation is tested under zero air (21% O_2 in N_2). Figure 8a is a schematic representation of the process for analyzing the soot oxidation activity. Briefly, the soot is mixed with the synthesized catalyst and then put in a TGA with an O_2 gas inlet. The soot oxidation profile in terms of percentage weight loss curve against temperature (in °C) is shown in Figure 8b. The light-off temperature at which 50% of the total weight loss occurs (T_{50}), and the temperature at inflection point (T_m) obtained from the derivative curve are used to study the temperature of maximal soot conversion rate where the CO_2 is maximum.[51] The T_{50} for bare soot (carbon black) oxidation without a catalyst is 746 °C (refer Figure S5). After the inclusion of catalyst, the temperature for 50% conversion is decreased to 644 °C for air annealed p-HfO_2 which further decreases for the hydrogenated HfO_2 to 632 °C for H-HfO_2_2h. Thus, it can be deduced that the presence of the HfO_2 catalyst accelerates the soot oxidation activity. Without the use of the catalyst, the onset temperature (T_{10}), at which 10% soot conversion takes place, is 699 °C, which is reduced to a range of (481−580 °C) in the presence of the HfO_2 (Table 5 and Figure 8c). The presence of HfO_2 decreases T_{50} by about (96−113) °C. Among all of the screened catalysts, p-HfO_2 showed the minimum T_{10} activity at 481 °C, while H-HfO_2_2h showed good catalytic performance, in which the T_{10} and T_{50} decreases by 148 and 113 °C, respectively. Thus, the soot conversion under the tight contact mode and in the presence of catalyst according to the T_{10} activity followed the trend p-HfO_2 < H_HfO_2_2h < H_HfO_2_10h < H_HfO_2_6h (Figure 8b). Catalyst incorporated soot oxidation experiments revealed that the T_m values decrease in chronological order: 663, 658, 649, and 636 °C for H-HfO_2_10h, p-HfO_2, H-HfO_2_6h, and H-HfO_2_2h, respectively. Although the onset temperature (T_{10}) is lowest for p- HfO_2, the peak temperature (T_m), light-off temperature (T_{50}), and the maximal conversion temperature (T_{90}) are lowest for the 2 h hydrogen annealed HfO_2. The good performance is attributed to higher surface adsorbed oxygen in the case of hydrogenated HfO_2 (as described above in Chemical Analysis). The active oxygen present for the soot conversion activity highly depends on the number of oxygen vacancies created upon the surface of the oxide material used.[52] Consequently, it is evident that the chemisorbed oxygen due to the surface adsorbed oxygen species present on the oxygen vacant sites contributed remarkably during the soot oxidation,

DOI: 10.1021/acssuschemeng.8b00674
ACS Sustainable Chem. Eng. 2018, 6, 11286−11294

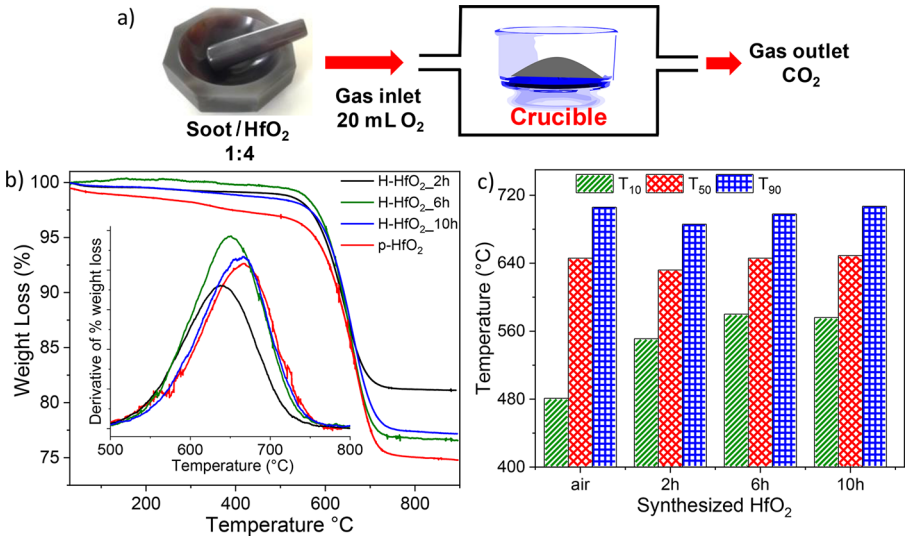

Figure 8. (a) Schematic representation of soot oxidation activity. (b) TGA profiles of carbon soot/HfO_2 mixtures (catalyst/soot ratio of 4:1) of different HfO_2 samples annealed in air and hydrogen, % weight loss curve and (8b, inset) derivative of weight loss function indicating oxidative peak profile. (c) Bar graph showing the T_{10}, T_{50}, and T_{90} temperatures in (°C) for all of the prepared samples; the values are indicated in Table 5.

Table 5. Catalytic Performance of the Prepared HfO_2 Samples Calculated Using TGA

sl. no.	HfO_2	T_m (°C)	T_{10} (°C)	T_{50} (°C)	T_{90} (°C)
1	p-HfO_2	658	481	644	706
2	H-HfO_2_2h	636	551	632	686
3	H-HfO_2_6h	649	580	646	698
4	H-HfO_2_10h	663	576	649	707
5	carbon	748	699	745	782

which agrees well with the XPS and O_2-TPD results as well. The durability of the catalyst is further tested by performing an accelerated thermal test. The catalyst is heated at 850 °C under humidified N_2 for 2 h followed by an oxidation cycle. The results are shown in Figure S6 and Table S3. The catalyst has been tested for five cycles and showed little loss of catalytic activity (Figure S7). Future studies will involve testing the optimized catalyst with other gaseous species such as H_2O, CO_x, NO_x, and hydrocarbons to understand the applicability of the catalyst in real conditions.

CONCLUSION

Although many innovative designs of materials for soot oxidation have been proposed over the years, it is the first for HfO_2 to be used as a catalytic material. Herein this study, efforts have been made to demonstrate a facile method for synthesizing HfO_2 nanoaggregates, the textural and structural properties of which can be changed by hydrogen annealing. Analysis using various techniques revealed the effect of hydrogen annealing, which was identified to cause increased lattice strain and visible expansion of the nanoaggregates in the TEM images, giving rise to its porous nature and strongly affecting the surface and binding of adsorbates, which was further confirmed by BET. In addition, XPS and O_2-TPD analysis observed a higher percentage of surface adsorbed oxygen compared to the lattice oxygen present, prompting good catalytic soot oxidation activity. This adsorbed surface oxygen desorbed at lower temperatures showed the labile nature of the active oxygen species involved during the oxidation reaction. Moreover, hydrogenation created higher oxygen vacant sites, increasing the possible generation of active oxygen species and the possibility to gain oxygen form the bulk of the materials and other gaseous sources. Thus, inert and stable HfO_2 nanomaterial can be effectively optimized by tuning its properties at lower temperature under reducing atmosphere. These nanomaterials can be further probed for properties like electrical and optical properties for use in various devices.

ASSOCIATED CONTENT

Supporting Information

The Supporting Information is available free of charge on the ACS Publications website at DOI: 10.1021/acssuschemeng.8b00674.

Figure S1: Pictorial representation of difference in color of p-HfO_2 and H-HfO_2 after annealing in H_2; Figure S2: XRD plot of change in 2θ with synthesis condition and strain plot calculated from Williamson Hall plot; Figure S3: Williamson Hall plot of all of the synthesized HfO_2 nanoaggregates; Figure S4: Plot of strain and catalytic activity; Figure S5: TGA graph of carbon showing T_{50}; Figure S6: Comparison TGA plot with and without accelerated thermal test (ATT); Figure S7: Reusability test of all of the synthesized HfO_2 nanoaggregates; Table S1: Literature survey of materials used for soot oxidation activity; Table S2: O_2-TPD measurement parameters of all of the synthesized nanomaterials; Table S3: TGA parameters of the synthesized nanomaterials with and without ATT (PDF)

AUTHOR INFORMATION

Corresponding Authors

*E-mail: ritu@iitj.ac.in (RG)
*E-mail: rks@iitj.ac.in (RKS)

ORCID

Ritu Gupta: 0000-0001-6819-2748
Rakesh K. Sharma: 0000-0002-0984-8281

Notes

The authors declare no competing financial interest.

DOI: 10.1021/acssuschemeng.8b00674
ACS Sustainable Chem. Eng. 2018, 6, 11286−11294

■ ACKNOWLEDGMENTS

DL and KPS acknowledge MHRD, Government of India, for providing financial assistance during research. RKS gratefully acknowledges the Indo-Portuguese bilateral research grant INT/Portugal/P-02/2013. Authors acknowledge MNIT Jaipur for TEM & XPS facilities, IIP Deharadun for TPD analysis and IIT Jodhpur CASE facility. RG thanks IIT Jodhpur for SEED grant.

■ REFERENCES

(1) Curtis, C. E.; Doney, L. M.; Johnson, J. R. Some Properties of Hafnium Oxide, Hafnium Silicate, Calcium Hafnate, and Hafnium Carbide. *J. Am. Ceram. Soc.* **1954**, *37* (10), 458−465.
(2) Wilk, G. D.; Wallace, R. M.; Anthony, J. M. High-κ gate dielectrics: Current Status and Materials Properties Considerations. *J. Appl. Phys.* **2001**, *89* (10), 5243−5257.
(3) Robertson, J. High Dielectric Constant Gate Oxides for Metal Oxide Si Transistors. *Rep. Prog. Phys.* **2006**, *69*, 327−396.
(4) Chow, R.; Falabella, S.; Loomis, G. E.; Rainer, F.; Stolz, C. J.; Kozlowski, M. R. Reactive Evaporation of Low-Defect Density Hafnia. *Appl. Opt.* **1993**, *32* (28), 5567−5574.
(5) Waldorf, A. J.; Dobrowolski, J. A.; Sullivan, B. T.; Plante, L. M. Optical Coatings Deposited by Reactive Ion Plating. *Appl. Opt.* **1993**, *32* (28), 5583−5594.
(6) Toledano-Luque, M.; San Andrés, E.; del Prado, A. d.; Mártil, I.; Lucía, M. L.; González-Díaz, G.; Martínez, F. L.; Bohne, W.; Röhrich, J.; Strub, E. High-Pressure Reactively Sputtered HfO_2: Composition, Morphology, and Optical Properties. *J. Appl. Phys.* **2007**, *102*, 044106.
(7) Wang, Y.; Lin, Z.; Cheng, X.; Xiao, H.; Zhang, F.; Zou, S. Study of HfO_2 Thin Films Prepared by Electron Beam Evaporation. *Appl. Surf. Sci.* **2004**, *228*, 93−99.
(8) De Roo, J.; De Keukeleere, K.; Feys, J.; Lommens, P.; Hens, Z.; Van Driessche, I. Fast, Microwave-Assisted Synthesis of Monodisperse HfO_2 Nanoparticles. *J. Nanopart. Res.* **2013**, *15*, 1778.
(9) Ferrari, S.; Modreanu, M.; Scarel, G.; Fanciulli, M. X-Ray Reflectivity and Spectroscopic Ellipsometry as Metrology Tools for the Characterization of Interfacial Layers in High-κ Materials. *Thin Solid Films* **2004**, *450*, 124−127.
(10) Villanueva-Ibanez, M.; Le Luyer, C.; Parola, S.; Marty, O.; Mugnier, J. Structural and Optical Properties of Eu^{3+}: HfO_2 Nanothick Sol-Gel Waveguiding Films. *Rev. Adv. Mater. Sci.* **2003**, *5*, 296−301.
(11) Matsumoto, K.; Itoh, Y.; Kameda, T. EB-PVD Process and Thermal Properties of Hafnia-Based Thermal Barrier Coating. *Sci. Technol. Adv. Mater.* **2003**, *4* (2), 153−158.
(12) Singh, J.; Wolfe, D. E.; Miller, R. A.; Eldridge, J. I.; Zhu, D.-M. Tailored Microstructure of Zirconia and Hafnia-based Thermal Barrier Coatings with Low Thermal Conductivity and High Hemispherical Reflectance by EB-PVD. *J. Mater. Sci.* **2004**, *39*, 1975−1985.
(13) Kingon, A. I.; Maria, J.-P.; Streiffer, S. K. Alternative Dielectrics to Silicon Dioxide for Memory and Logic Devices. *Nature* **2000**, *406*, 1032−1038.
(14) Rinkiö, M.; Johansson, A.; Paraoanu, G. S.; Törmä, P. High-Speed Memory from Carbon Nanotube Field-Effect Transistors with High-κ Gate Dielectric. *Nano Lett.* **2009**, *9* (2), 643−647.
(15) Al-Bahar, F.; Collins, D. J.; Watters, J. C.; Davis, B. H. Catalytic Conversion of Alcohols. 12. Selectivity of Hafnium Oxide. *Ind. Eng. Chem. Prod. Res. Dev.* **1979**, *18* (3), 199−202.
(16) De Roo, J. D.; Van Driessche, I. V.; Martins, J. C.; Hens, Z. Colloidal Metal Oxide Nanocrystal Catalysis by Sustained Chemically Driven Ligand Displacement. *Nat. Mater.* **2016**, *15*, 517−521.
(17) Sahraneshin, A.; Asahina, S.; Togashi, T.; Singh, V.; Takami, S.; Hojo, D.; Arita, T.; Minami, K.; Adschiri, T. Surfactant-Assisted Hydrothermal Synthesis of Water-Dispersible Hafnium Oxide Nanoparticles in Highly Alkaline Media. *Cryst. Growth Des.* **2012**, *12* (11), 5219−5226.
(18) Wan, Y.; Zhou, X. Formation Mechanism of Hafnium Oxide Nanoparticles by a Hydrothermal Route. *RSC Adv.* **2017**, *7*, 7763−7773.
(19) Xiang, L.; Yin, Y. P.; Jin, Y. Hydrothermal Formation of Ni-Zn Ferrite from Heavy Metal Co-Precipitates. *J. Mater. Sci.* **2002**, *37*, 349−352.
(20) Yin, H.; Wada, Y.; Kitamura, T.; Kambe, S.; Murasawa, S.; Mori, H.; Sakata, T.; Yanagida, S. Hydrothermal Synthesis of Nanosized Anatase and Rutile TiO_2 using Amorphous Phase TiO_2. *J. Mater. Chem.* **2001**, *11*, 1694−1693.
(21) Zheng, Y. Q.; Shi, E.; Chen, Z.; Li, W.; Hu, X. Influence of Solution Concentration on the Hydrothermal Preparation of Titania Crystallites. *J. Mater. Chem.* **2001**, *11*, 1547−1551.
(22) Lee, M.-C. M.; Wu, M. C. Thermal Annealing in Hydrogen for 3-D Profile Transformation on Silicon-on Insulator and Sidewall Roughness Reduction. *J. Microelectromech. Syst.* **2006**, *15* (2), 338−343.
(23) Al-Kuhaili, M. F.; Durrani, S. M. A.; Bakhtiari, I. A.; Dastageer, M. A.; Mekki, M. B. Influence of Hydrogen Annealing on the Properties of Hafnium Oxide Thin Films. *Mater. Chem. Phys.* **2011**, *126*, 515−523.
(24) Wagloehner, S.; Baer, J. N.; Kureti, S. Structure−Activity Relation of Iron Oxide Catalysts in Soot Oxidation. *Appl. Catal., B* **2014**, *147* (5), 1000−1008.
(25) Guo, X.; Meng, M.; Dai, F.; Li, Q.; Zhang, Z.; Jiang, Z.; Zhang, S.; Huang, Y. NOx-Assisted Soot Combustion over Dually Substituted Perovskite Catalysts $La_{1-x}K_xCo_{1-y}Pd_yO_{3-\delta}$. *Appl. Catal., B* **2013**, *142−143*, 278−289.
(26) Giménez-Mañogil, J.; Bueno-López, A.; García-García, A. Preparation, characterisation and testing of $CuO/Ce_{0.8}Zr_{0.2}O_2$ catalysts for NO oxidation to NO_2 and mild temperature diesel soot combustion. *Appl. Catal., B* **2014**, *152−153*, 99−107.
(27) Reddy, B. M.; Bharali, P.; Saikia, P.; Khan, A.; Loridant, S. p.; Muhler, M.; Grünert, W. Hafnium Doped Ceria Nanocomposite Oxide as a Novel Redox Additive for Three-Way Catalysts. *J. Phys. Chem. C* **2007**, *111* (5), 1878−1881.
(28) Reddy, B. M.; Bharali, P.; Thrimurthulu, G.; Saikia, P.; Katta, L.; Park, S.-E. Catalytic Efficiency of Ceria−Zirconia and Ceria−Hafnia Nanocomposite Oxides for Soot Oxidation. *Catal. Lett.* **2008**, *123*, 327−333.
(29) Laishram, D.; Shejale, K. P.; Sharma, R. K.; Gupta, R. HfO_2 Nanodots Incorporated in TiO_2 and its Hydrogenation for High Performance Dye Sensitized Solar Cells. *RSC Adv.* **2016**, *6*, 78768−78773.
(30) Reddy, B. M.; Bharali, P.; Saikia, P.; Khan, A.; Loridant, S.; Muhler, M.; Grünert, W. Hafnium Doped Ceria Nanocomposite Oxide as a Novel Redox Additive for Three-Way Catalysts. *J. Phys. Chem. C* **2007**, *111* (5), 1878−1881.
(31) Ramana, C. V.; Bharathi, K. K.; Garcia, A.; Campbell, A. L. Growth Behavior, Lattice Expansion, Strain, and Surface Morphology of Nanocrystalline, Monoclinic HfO_2 Thin Films. *J. Phys. Chem. C* **2012**, *116*, 9955−9960.
(32) Hosseinpour, P. M.; Yung, D.; Panaitescu, E.; Heiman, D.; Menon, L.; Budil, D.; Lewis, L. H. Correlation of Lattice Defects and Thermal Processing in the Crystallization of Titania Nanotube Arrays. *Mater. Res. Express* **2014**, *1*, 045018.
(33) Chaubey, G. S.; Yao, Y.; Makongo, J. P. A.; Sahoo, P.; Misra, D.; Poudeu, P. F. P.; Wiley, J. B. Microstructural and Thermal Investigations of HfO_2 Nanoparticles. *RSC Adv.* **2012**, *2* (24), 9207−9213.
(34) Anwar, T.; Li, W.; Hussain, N.; Chen, W.; Ur Rehman Sagar, R. U.; Tongxiang, L. Effect of Annealing Atmosphere Induced Crystallite Size Changes on the Electrochemical Properties of TiO_2 Nanotubes Arrays. *Journal of Electrical Engineering* **2016**, *4*, 43−51.
(35) Uvarov, V.; Popov, I. Metrological characterization of X-Ray Diffraction Methods at Different Acquisition Geometries for Determination of Crystallite Size in Nano-Scale Materials. *Mater. Charact.* **2013**, *85*, 111−123.

DOI: 10.1021/acssuschemeng.8b00674
ACS Sustainable Chem. Eng. 2018, 6, 11286−11294

(36) Nayak, N. B.; Nayak, B. B. Temperature-Mediated Phase Transformation, Pore Geometry and Pore Hysteresis Transformation of Borohydride Derived In-Born Porous Zirconium Hydroxide Nanopowders. *Sci. Rep.* **2016**, *6*, 26404.
(37) Lowell, S.; Shields, J. E.; Thomas, M. A.; Thommes, M. *Characterization of Porous Solids and Powders: Surface Area, Pore Size and Density*; Kluwer Academic Publishers: The Netherlands, 2004.
(38) Hwang, N.; Barron, A. R. *BET Surface Area Analysis of Nanoparticles*. http://cnx.org/contents/9cBY4EHy@1/BET-Surface-Area-Analysis-of-N (accessed July 2017).
(39) Grosman, A.; Ortega, C. Capillary Condensation in Porous Materials. Hysteresis and Interaction Mechanism without Pore Blocking/Percolation Process. *Langmuir* **2008**, *24*, 3977−3986.
(40) Nguyen, P. T. M.; Fan, C.; Do, D. D.; Nicholson, D. On the Cavitation-Like Pore Blocking in Ink-Bottle Pore: Evolution of Hysteresis Loop with Neck Size. *J. Phys. Chem. C* **2013**, *117*, 5475−5484.
(41) Sing, K. S. W.; Williams, R. T. Physisorption Hysteresis Loops and the Characterization of Nanoporous Materials. *Adsorpt. Sci. Technol.* **2004**, *22* (10), 773−782.
(42) Lin, S.-S.; Liao, C.-S. Structure and Physical Properties of W-Doped HfO_2 Thin Films Deposited by Simultaneous RF and DC Magnetron Sputtering. *Surf. Coat. Technol.* **2013**, *232*, 46−52.
(43) Suzer, S.; Sayan, S.; Banaszak Holl, M. M.; Garfunkel, E.; Hussain, Z.; Hamdan, N. M. Soft X-Ray Photoemission Studies of Hf Oxidation. *J. Vac. Sci. Technol., A* **2003**, *21* (1), 106−109.
(44) Barreca, D.; Milanov, A.; Fischer, R. A.; Devi, A.; Tondello, E. Hafnium oxide thin film grown by ALD: An XPS study. *Surf. Sci. Spectra* **2007**, *14* (1), 34−40.
(45) Fan, L.; Xi, K.; Zhou, Y.; Zhu, Q.; Chen, Y.; Lu, H. Design Structure for CePr Mixed Oxide Catalysts In Soot Combustion. *RSC Adv.* **2017**, *7* (33), 20309−20319.
(46) Zhang, W.; Niu, X.; Chen, L.; Yuan, F.; Zhu, Y. Soot Combustion over Nanostructured Ceria with Different Morphologies. *Sci. Rep.* **2016**, *6*, 29062.
(47) Liang, Q.; Wu, X.; Weng, D.; Xu, H. Oxygen Activation on Cu/Mn−Ce Mixed Oxides and the Role in Diesel Soot Oxidation. *Catal. Today* **2008**, *139*, 113−118.
(48) Fu, M.; Yue, X.; Ye, D.; Ouyang, J.; Huang, B.; Wu, J.; Liang, H. Soot Oxidation via CuO Doped Ceo_2 Catalysts Prepared Using Coprecipitation and Citrate Acid Complex-Combustion Synthesis. *Catal. Today* **2010**, *153*, 125−132.
(49) Li, Y.; Du, Y.; Wei, Y.; Zhao, Z.; Jin, B.; Zhang, X.; Liu, J. Catalysts of 3D Ordered Macroporous ZrO_2-Supported Core−Shell Pt@CeO_{2-x} Nanoparticles: Effect of the Optimized Pt−CeO_2 Interface on Improving the Catalytic Activity and Stability of Soot Oxidation. *Catal. Sci. Technol.* **2017**, *7*, 968−981.
(50) Jampaiah, D.; Velisoju, V. K.; Venkataswamy, P.; Coyle, V. E.; Nafady, A.; Reddy, B. M.; Bhargava, S. K. Nanowire Morphology of Mono- and Bidoped α-MnO_2 Catalysts for Remarkable Enhancement in Soot Oxidation. *ACS Appl. Mater. Interfaces* **2017**, *9*, 32652−32666.
(51) Aneggi, E.; de Leitenburg, C.; Dolcetti, G.; Trovarelli, A. Promotional Effect of Rare Earths and Transition Metals in the Combustion of Diesel Soot Over CeO_2 and CeO_2−ZrO_2. *Catal. Today* **2006**, *114* (1), 40−47.
(52) Fino, D.; Bensaid, S.; Piumetti, M.; Russo, N. A Review on the Catalytic Combustion of Soot in Diesel Particulate Filters for Automotive Applications: from Powder Catalysts to Structured Reactors. *Appl. Catal., A* **2016**, *509*, 75−96.

DOI: 10.1021/acssuschemeng.8b00674
ACS Sustainable Chem. Eng. 2018, 6, 11286−11294